THE JOURNAL OF PHYSICAL CHEMISTRY LETTERS
A JOURNAL OF THE AMERICAN CHEMICAL SOCIETY

pubs.acs.org/JPCL Letter

Energy and Charge Transfer Dynamics in Red-Emitting Hybrid Organo-Inorganic Mixed Halide Perovskite Nanocrystals

I-Hua Tsai, Sudhakar Narra, Sumit S. Bhosale, and Eric Wei-Guang Diau*

Cite This: J. Phys. Chem. Lett. 2023, 14, 2580−2587 Read Online

ACCESS | Metrics & More | Article Recommendations | Supporting Information

ABSTRACT: We report time-resolved spectral properties of highly stable and efficient red-emitting hybrid perovskite nanocrystals with the composition $FA_{0.5}MA_{0.5}PbBr_{0.5}I_{2.5}$ (FAMA PeNC) synthesized by using the hot-addition method. The PL spectrum of the FAMA PeNC shows a broad asymmetric band covering 580 to 760 nm with a peak at 690 nm which can be deconvoluted into two bands corresponding to the MA and FA domains. The interactions between the MA and FA domains are shown to affect the relaxation dynamics of the PeNCs from the subpicosecond to tens of nanoseconds scale. Time-correlated single-photon counting (TCSPC), femtosecond PL optical gating (FOG), and femtosecond transient absorption spectral (TAS) techniques were employed to study the intercrystal energy transfer (photon recycling) and intracrystal charge transfer processes between the MA and the FA domains of the crystals. These two processes are shown to increase the radiative lifetimes for the PLQYs exceeding 80%, which may play a key role in enhancing the performance of PeNC-based solar cells.

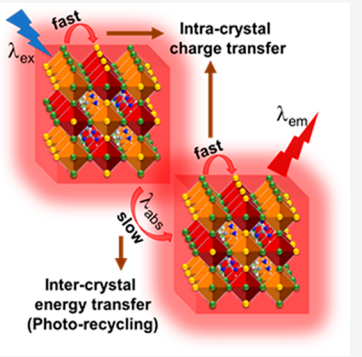

Perovskite nanocrystals (PeNCs) have been extensively studied for photovoltaic, optoelectronic, and photocatalytic applications in recent years due to the plethora of exotic photoelectronic properties of PeNC.[1−6] PeNCs can be synthesized using hot injection or addition, ligand-assisted reprecipitation, and top-down methods whose emissions can be tuned across the spectra by modulating the particle sizes (utilizing quantum confinements) and chemical compositions.[7−12] Perovskite materials are known for their highly overlapping absorption and emission spectra; as a result, photon recycling takes place due to the reabsorption of emitted photons.[13−16] Photon recycling is beneficial for solar cells as it can extend the carrier transport beyond the diffusion limit but it is detrimental to solar concentrators and light-emitting diodes due to the incurred nonradiative losses.[17−20]

The higher long-term stability and photon recycling behavior of PeNCs compared to those of their 3D counterparts have opened a new avenue for perovskite solar cells. The long-term stability of PeNCs comes from the protection offered by the surface ligands that wrap the crystals, whereas the photon recycling behavior is attributed to their broad band gap redistribution of small crystals. The band gap of the PeNCs designed to be utilized in solar cells is often a low band gap type with band edges that are longer than 700 nm.[21−23] Unfortunately, the red-emitting PeNCs are less stable with weaker emissions compared to the green-emitting PeNCs.[24,25] To stabilize the red-emitting PeNCs, the approach of mixed A-site cations using the hot injection method and postsynthetic treatments with quaternary ammonium salts has been followed to make the synthetic procedure cumbersome.[26,27] In our earlier work, we developed a facile one-pot synthesis approach named the hot addition method to synthesize highly stable and efficient PeNCs with emissions at 630 nm suitable for optoelectronic applications.[28] In this work, using the same approach, we successfully tuned the emission of the PeNCs to 690 nm by mixing the A-site cations with methylammonium (MA) and formamidinium (FA) cations and mixing iodide with bromide to synthesize the PeNC with the composition $FA_{0.5}MA_{0.5}PbBr_{0.5}I_{2.5}$ (FAMA PeNC). The synthesized FAMA PeNCs are shown to display a small size and a narrow size distribution but broad emission coverage with excellent stability and photoluminescence quantum yields (PLQYs) exceeding 80% upon shelf storage over 30 days. Furthermore, these FAMA PeNCs display excellent photon recycling properties according to the results obtained from time-correlated single-photon-counting (TCSPC) measurements. Femtosecond emission optical gating (FOG) and transient absorption spectral (TAS) studies were carried out to understand the effects of intracharge transfer processes. The intracharge transfer occurred between the donor MA (high energy) domain and the acceptor FA (low energy) domain of the nanocrystals on two time scales: the hot-carrier cooling and band gap renormalization occurred in ∼0.4 ps whereas the cold-carrier charge transfer from the MA to the FA domain

Received: February 3, 2023
Accepted: March 3, 2023

https://doi.org/10.1021/acs.jpclett.3c00333
J. Phys. Chem. Lett. 2023, 14, 2580−2587

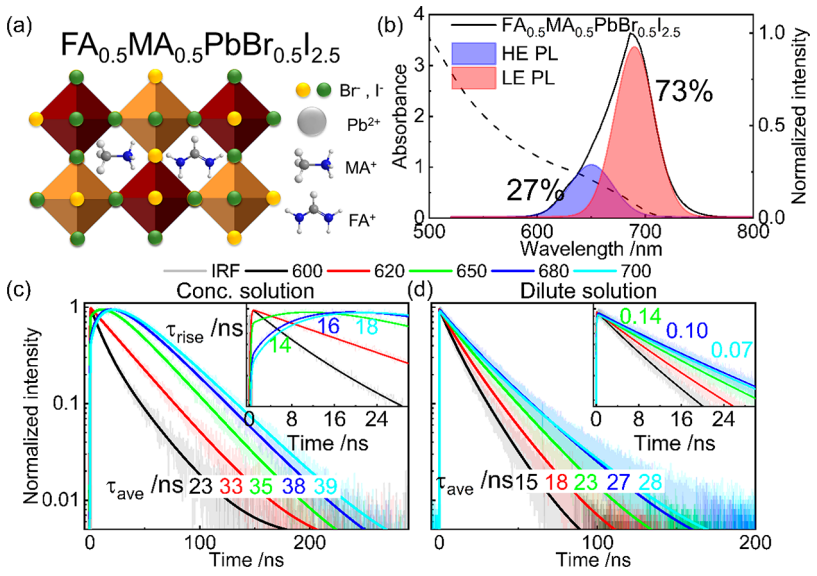

Figure 1. (a) Chemical structure of hybrid $FA_{0.5}MA_{0.5}PbBr_{0.5}I_{2.5}$ (FAMA) PeNC and (b) UV−vis (dashed curve) and PL spectra of FAMA PeNC. The PL spectrum is deconvoluted by fitting with two Gaussian bands as indicated. (c, d) Time-correlated single-photon-counting (TCSPC) decay profiles of as-prepared (concentrated) and diluted FAMA PeNC suspension solutions monitored at 600, 620, 650, 680, and 700 nm in varied colors as indicated. The decay profiles were fitted with rise and multiple decay exponential functions. Complete fit coefficients can be found in Tables S2 and S3. Only rise times and average lifetimes are shown here.

occurred in 30 ps. The shallow-trap-mediated recombination occurred in 10 ps in both MA and FA domains while the bulk-trap-mediated recombination occurred in 60 and 140 ps in MA and FA domains, respectively. Both FOG and TAS transients exhibit a nanosecond-offset component corresponding to the radiative recombination in tens of nanoseconds determined by the TCSPC measurements.

The hybrid organo-inorganic mixed halide lead perovskite $FA_{0.5}MA_{0.5}PbBr_{0.5}I_{2.5}$ nanocrystals were synthesized using the hot-addition method reported elsewhere.[28] The detailed synthetic procedures are described in the Supporting Information (SI). Briefly, methylammonium iodide (MAI), formamidinium bromide (FABr), and lead iodide (PbI_2) are taken in a 1:1:1 ratio to form FAMA PeNC with the crystal composition $FA_{0.5}MA_{0.5}PbBr_{0.5}I_{2.5}$. The transmission electron micrograph (TEM) image (Figure S1) of FAMA PeNC shows a uniform arrangement of the nanocrystals with a narrow size distribution; the average particle size was determined to be 10.7 ± 3.4 nm. The XRD patterns of FAMA PeNC (Figure S2a) show intense and broad XRD peaks at 14 and 28°, which can be well simulated with the standard $FAPbI_3$ and $MAPbI_3$ XRD patterns following the Rietveld refinement procedure using total pattern analysis solutions (TOPAS) software (Figure S2b); the TOPAS simulation yielded a 51.7% tetragonal structure (MA domain) and 48.3% cubic structure (FA domain) for FAMA PeNC. The similar proportions of tetragonal and cubic structures obtained from the XRD simulations indicate the successful incorporation of both MA and FA cations in equal proportions into the PeNC as the crystal structure shown in Figure 1a. It is worth noting that tweaking the ratio between FABr and MAI led to the poor colloidal stability of the synthesized PeNCs. The poor colloidal stability can be partially attributed to their tolerance factors[29,30] falling outside the ideal range of 0.94−0.98 (Table S1). Therefore, we will focus on the photophysical studies of only the FAMA PeNC with an equal molar ratio of FA/MA in this work; the corresponding results are shown in Figures S2−S9 with the fitted parameters summarized in Tables S2−S10.

The absorption spectrum of FAMA PeNC (dashed curve in Figure 1b) displays a continuous band with a band edge at 710 nm, whereas the excitonic absorption band was not observed in the spectrum, which is often the case for larger crystals with small exciton binding energies.[31,32] The PL spectrum of PeNC (Figure 1b) shows a broad emission band spanning the range of 580−760 nm with a peak maximum at 690 nm. The broad PL spectrum was deconvoluted by fitting with two Gaussian functions, as shown in Figure 1b. The deconvoluted high-energy (HE) and low-energy (LE) PL bands show proportions of 27 and 73% of the total PL band area for the former and latter PL bands, respectively. The HE and LE PL bands should represent either the different proportions of organic cations or those of the halide ions. Usually, I-rich spectra show a red-shifted spectral feature when compared with the Br-rich spectra,[33,34] but in our case, iodine is much richer than bromine inside the PeNC. To assign the HE and LE PL bands, the MAI concentration was slightly increased as a drastic change in the MA component would lead to poor stability of the nanocrystals as mentioned earlier. The PL spectrum of the MA-rich sample (Figure S3) shows an increase in the band intensity on the blue side of the spectrum without displaying any peak shift. Therefore, the HE PL band is assigned to the MA domain, and the LE PL band is assigned to the FA domain of the PeNC. Furthermore, the synthesized hybrid FAMA PeNCs display remarkable PLQYs of between 80 and 90% with good stability for more than 30 days as shown in Figure S4.

The PL decay profiles of the hybrid FAMA PeNC shown in Figures 1c (concentrated sample) and 1d (diluted sample) were obtained by exciting the samples using a 375 nm picosecond excitation pulse (pulse width ∼80 ps), and the decay profiles were monitored at varied wavelengths of the PL spectrum as indicated in the figure captions using the TCSPC technique. The HE PL band decay profiles at 600 and 620 nm

https://doi.org/10.1021/acs.jpclett.3c00333
J. Phys. Chem. Lett. 2023, 14, 2580−2587

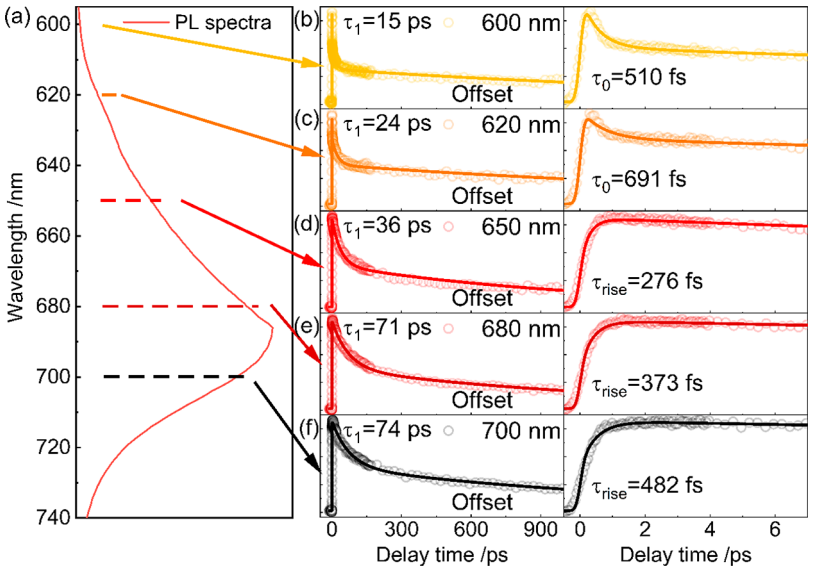

Figure 2. (a) PL spectrum and (b–f) femtosecond PL decay profiles of $FA_{0.5}MA_{0.5}PbBr_{0.5}I_{2.5}$ PeNC suspensions. The excitation wavelength was set to 400 nm. The PL decay profiles at 600, 620, 650, 680, and 700 nm bands were fitted with a rise and a decay exponential function with a nanosecond offest; the corresponding fitted time coefficients are displayed in the legends. Fitted decay coefficients are shown in Table S6.

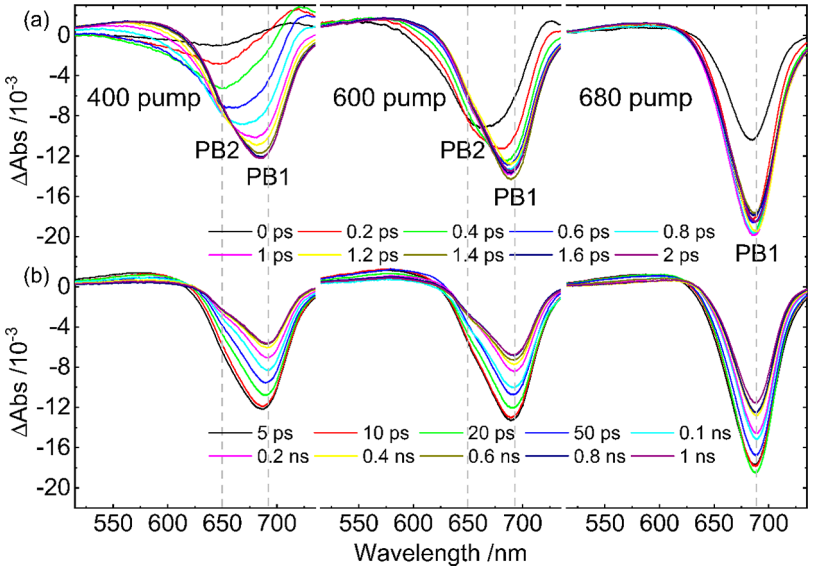

Figure 3. Femtosecond transient absorption spectra of the $FA_{0.5}MA_{0.5}PbBr_{0.5}I_{2.5}$ PeNC suspension sample under 400, 600, and 680 nm excitations. The top panel shows spectral evolutions in the 0–2 ps region, while the bottom panel shows spectral evolutions in the 5 ps–1 ns region.

show rapid decays, whereas the LE PL band decay profiles at 680 and 700 nm show a slow rise and slow decays on the nanosecond time scale for the concentrated (as-prepared) PeNC sample shown in Figure 1c. In contrast, the 50-fold diluted sample (Figure 1d) showed very rapid rise components on the picosecond scale, and the average decay coefficients were also observed to be faster than those of concentrated sample on the nanosecond scale. The PL spectrum of the PeNC sample shown in Figure 1b exhibits strong overlap with the absorption spectrum; specifically, the deconvoluted HE PL band is mostly buried in the sample's absorption band. Thus, it is likely that the observed slow rise in the concentrated sample is due to the photon recycling caused by the reabsorption of the emitted photons by the close-lying neighboring crystals, for which the rise contribution in the PL transients is suppressed in the case of a diluted sample. Furthermore, the effects of photon recycling on the decay kinetics were confirmed by reducing the path lengths of the sample cell holder as shown in Figure S5. (Fitted kinetic parameters are shown in Tables S4 and S5.) The photon recycling was suppressed as the optical path length was decreased from 10 to 1 and 0.1 mm as evidenced by the absence of a nanosecond rise component in the PL transients of the thinner samples.

There are two important points to be mentioned for the observations. First, the rise time coefficients in the diluted and thinner samples are much shorter than those in the concentrated and thicker sample. Second, the decay time coefficients are also shorter for the diluted and thinner samples than for the concentrated and thicker sample. These observations indicate that the intercrystal interaction between the MA and FA domains of the nanocrystal was involved in the concentrated and thicker sample but such an interaction was

https://doi.org/10.1021/acs.jpclett.3c00333
J. Phys. Chem. Lett. 2023, 14, 2580–2587

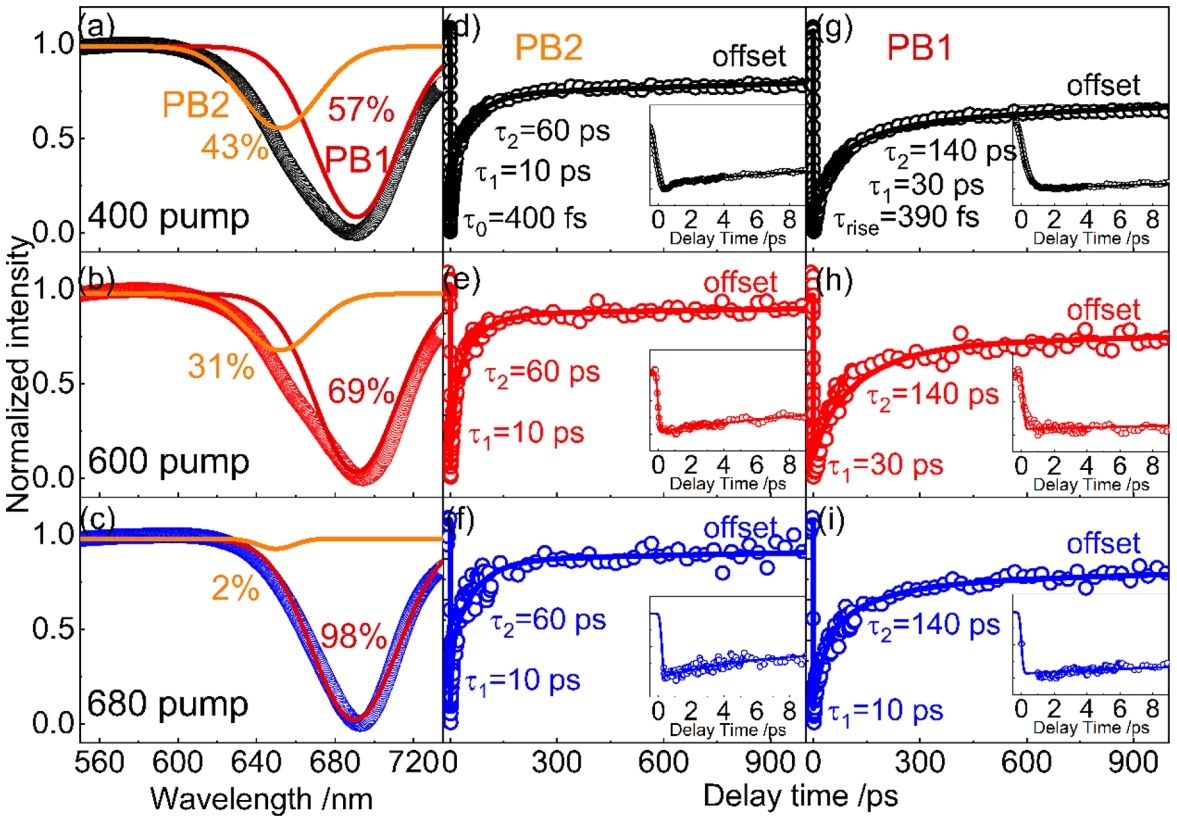

Figure 4. (a–c) Femtosecond transient absorption spectra of the $FA_{0.5}MA_{0.5}PbBr_{0.5}I_{2.5}$ PeNC suspension sample monitored at 2 ps with excitation at 400, 600, and 680 nm. The spectral profiles were deconvoluted by fitting with two Gaussian functions indicated as PB2 and PB1 bands. Transient profiles were recorded at (d–f) 650 nm and (g–i) 690 nm representing the relaxation dynamics at PB2 and PB1 bands, respectively. The transient curves were fitted with rise (400 nm excitation) and decay exponential functions with fitted time coefficients as indicated. Complete fitting parameters are shown in Table S7.

diminished in the diluted and thinner samples as the nanosecond rise component was absent for the latter. The intercrystal energy transfer in the concentrated and thicker sample also led to a strong dipole–dipole interaction between the two nearby nanocrystals that slows down its nanosecond decay kinetics as shown in Figure 1c. Such an intercrystal energy transfer is the result of photon recycling that enhances the nanosecond decay coefficient responsible for the greater radiative recombination to enhance the observed high PLQYs shown in Figure S4. The observed pulse-limited picosecond-rise component in the diluted and thinner samples might be due to the charge transfer inside the crystal (intracrystal interaction), which will be investigated by the femtosecond (fs) spectral techniques detailed in what follows.

The femtosecond-PL decay profiles of the as-prepared PeNC sample were obtained by upconverting the emission signals using the FOG technique. The excitation wavelength was set to 400 nm, and the decay profiles were recorded along the PL emission spectrum from 600 to 700 nm as shown in Figure 2. The path length of the cell was set to 1 mm to minimize the photon recycling events so as to catch the evolution dynamics of intracrystal charge transfer between donor (MA) and acceptor (FA) domains while performing the femtosecond-PL upconversion measurements. At the PL wavelengths of 600 and 620 nm when the PL signals mostly came from the MA domain, the femtosecond-PL decay profiles show two rapid decay components with subpicosecond and ps time coefficients, respectively, along with a nanosecond-offset component associated with the radiative decay. At the PL wavelengths of 650–700 nm, the rapid subpicosecond decay component disappeared; instead, a rapid subpicosecond rise component appeared. Therefore, we assign the subpicosecond components as intracrystal charge transfer of the hot carriers from the MA to the FA domain. Note that the time coefficients of all components increase upon increasing the probe wavelength because of the detection window which is broader at the longer wavelengths than at the shorter wavelengths.[35] In other words, more relaxed species can be probed at longer wavelengths than those at shorter wavelengths. The picosecond components are assigned to the crystal relaxation to the defect states, for which the PL signals probed at 600 and 620 show much more rapid defect relaxation in the MA domain than those at 680 and 700 nm in the FA domain showing the similar defect relaxation from the thermalized cold carriers.

To clearly ascertain the ultrafast relaxation between the donor (MA) and acceptor (FA) domains, experiments at varied pump wavelengths were performed using the femtosecond TAS technique as resonant excitation experiments are quite challenging using the aforementioned FOG technique. The TAS experiments were performed using three different pump wavelengths, namely, 400, 600, and 680 nm, while the probing window was set to the 510–730 nm spectral region. The pump wavelengths at 600 and 680 nm are in resonance with the PL emission bands of MA and FA domains of the nanocrystal, respectively, whereas excitation at 400 nm is the excess-energy excitation that resembles that of the FOG and TCSPC decay measurements. The TAS profiles of the FAMA PeNC show a photobleach (PB) band at the 690 nm peak

https://doi.org/10.1021/acs.jpclett.3c00333
J. Phys. Chem. Lett. 2023, 14, 2580–2587

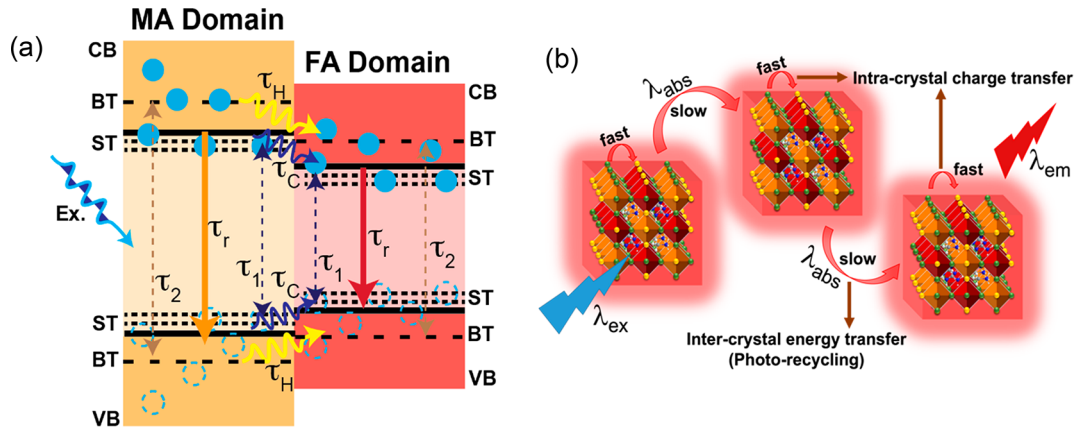

Figure 5. (a) Ultrafast carrier relaxation model and (b) slow photon recycling mediated by intracrystal energy transfer and rapid intercrystal charge transfer processes in $FA_{0.5}MA_{0.5}PbBr_{0.5}I_{2.5}$ PeNCs. Abbreviations: VB, valence band; CB, conduction band; BT, bulk-trap states; and ST, shallow-trap states.

associated with the depletion of the band-edge states under all excitation conditions. The PB band of PeNCs shows broadening and spectral shifts under 400 and 600 nm excitations, while the 680 nm excitation shows relatively sharper bands without a specific transient spectral shift. The transient spectral shifts and the band broadening observed on the TAS profiles from the 400 and 600 nm excitations are due to the cumulative results of band gap renormalization (BGR), hot carrier cooling, and band filling (BF) effects.[36−39] The BGR can be evidenced from the significant blue shifts of the TAS bands following photoexcitation, and then the transient bands were propagated from 650 nm toward 680 nm when the time delay between pump and probe pulses proceeded. The hot carrier cooling signatures can be visualized from the asymmetrically broadened PB tails on the blue side of the transient spectrum with a photoinduced absorption (PIA) band on the red side of the spectrum at an early time delay. The BF effect can be seen from the blue shift of the PB bands at 5 ps compared to the 1 ns spectrum for 400 and 600 nm excitations.

The TAS profiles show broader and slightly asymmetric features even after the hot carrier cooling and BGR processes become complete after 2 ps. Thus, the TAS profiles obtained at 2 ps under different excitation conditions were deconvoluted by fitting with two Gaussian functions as shown in Figure 4a−c for 400, 600, and 680 excitations, respectively. The spectral components representing the FA (690 nm) and MA (650 nm) domains of the nanocrystal are labeled as PB1 and PB2 bands, respectively. The integrated area of the PB2 band was 43% upon 400 nm excitation, but it decreases to 31 and 2% upon excitation at 600 and 680 nm, respectively. This indicates that more donor states in the MA domain were excited under 400 nm excitation than under 600 nm excitation. At 680 nm excitation, only FA-domain species of the nanocrystals were excited.

The transient temporal profiles at varied excitation wavelengths for the PB2 (650 nm) and PB1 (690 nm) bands are displayed in Figure 4d−f and 4g−i, respectively. The transient profiles were fitted with a Gaussian function (IRF) convoluted with multiexponential functions. The kinetics of the PB2 band display decays of 10 (τ_1) and 60 (τ_2) ps together with a nanosecond-offset component. We assign τ_1, τ_2, and the nanosecond offset to be associated with processes of shallow trap, bulk trap, and radiative recombination, respectively.[40]

Similarly, the transient kinetics of the PB1 band display τ_1 (30 ps), τ_2 (140 ps), and the nanosecond offset for 400 and 600 nm excitations. Note that for the 680 nm excitation, no MA-domain species was excited, and the shallow-trap-mediated recombination (τ_1) occurred in 10 ps as probed at 690 nm (Figure 4i), the same as those of PB2 band relaxation probed in the MA domain. Therefore, we assign the time coefficient for the intrinsic shallow-trap-mediated recombination to be 10 ps for the nanocrystals in both MA and FA domains. When the FAMA PeNC was excited at 400 and 600 nm, both τ_1 values appeared to be 30 ps in the FA domain (690 nm). Since intrinsic shallow-trap-mediated recombination occurs in 10 ps, the observed 30 ps decay in the FA domain for both 400 and 600 nm excitations must come from a slow bottleneck process, for which we assign this to be the charge-transfer process from MA to the FA domain. In addition, at 400 nm excitation, the PB2 band relaxation exhibits a small 400 fs decaying component (inset of Figure 4d). In contrast, lacking the rapid-decay component, the PB1 band relaxation displays a 390 fs rise component under 400 nm excitation. Thus, the rise of the subpicosecond component of PB1 and the decay of the subpicosecond component of PB2 confirm the existence of intracrystal hot-carrier transfer from the PB2 band (MA domain) to the PB1 band (FA domain) with a time coefficient of $\tau_H \approx 0.4$ ps. This hot-carrier charge transfer feature is further confirmed by probing the transient profiles from 650 to 720 nm in the short-time region for both FOG and TAS experiments (Figures S6 and S7).

The subpicosecond component (τ_H) reflects the charge transfer of the hot carriers from the MA to the FA domain, whereas the 30 ps component (τ_C) reflects the charge transfer of the cold carriers in the shallow trap states from the MA to the FA domain. It is interesting that bulk-trap states are not involved in the charge transfer between MA and FA domains. As shallow-trap states are often in thermal equilibrium with the conduction band,[41] their recombination rates can affect the radiative recombination rates. Thus, the observed slower radiative recombination in the TCSPC decays for the FA domain (LE PL band) rather than for the MA domain (HE PL band) could be due to the shallow-trap recombination caused by charge transfer from the MA domain to the FA domain. Furthermore, both FOG and TAS experiments show similar wavelength-dependent rise times (Figures S6), but their decay profiles show different time coefficients due to the comple-

https://doi.org/10.1021/acs.jpclett.3c00333
J. Phys. Chem. Lett. 2023, 14, 2580−2587

mentary nature of the experiments and differences in detection windows between these two techniques. One question remained to be answered for the competition between shallow-trap-mediated recombination (~10 ps) and cold-carrier charge transfer (~30 ps). Note that the former occurs in the bulk MA domain while the latter occurs in the interface between MA and FA domains. Even though the shallow-trap recombination is much faster, there is a certain dipole−dipole interaction to form excitons in the MA−FA interface for the interfacial charge transfer to occur slowly, and this slows down the relaxation kinetics observed in the FA-domain window upon both 400 and 600 nm excitations.

Finally, the relaxation mechanism in the hybrid FAMA PeNC is presented in Figure 5 on the basis of the observed kinetics using the TCSPC, FOG, and femtosecond-TAS techniques reported herein. Upon excitation at 400 and 600 nm under the conditions of a diluted solution or thinner cell holder, both MA and FA domains of the nanocrystals were excited. As shown in Figure 5a, intracrystal charge transfer occurs from the MA domain to the FA domain on two time scales: hot-carrier charge transfer occurs in ~0.4 ps (τ_H) whereas cold-carrier charge transfer occurs in ~30 ps (τ_C). Meanwhile, the charge recombination occurs on three time scales: For the MA domain, the shallow-trap-mediated recombination occurs in 10 ps (τ_1) while the bulk-trap-mediated recombination occurs in 60 ps (τ_2), and the radiative recombination is responsible for the nanoseond-offset signals (τ_r) observed in both FOG and TAS experiments. For the FA domain, the shallow-trap-mediated recombination occurs in 10 ps (τ_1) while the bulk-trap-mediated recombination occurs in 140 ps (τ_2) together with a nanosecond offset responsible for the radiative recombination (τ_r). The differences in the time coefficients of the bulk-trap-mediated recombination processes for MA and FA domains could be due to different bulk-type defects formed locally by the respective organic cations for which more defects are expected for the MA domain than for the FA domain (60 vs 140 ps). This is not the case for the shallow-trap-state-mediated recombination processes as they are often formed by halogen vacancies. As shown in Figure 5b, photon recycling due to the reabsorption of emitted photons occurs when the PeNCs come closer in a concentrated solution or in a thick cell holder. In earlier works, exciton hopping due to Forster type energy transfer has been shown to be responsible for the photon-recycling process in the green-emitting PeNCs.[16] Therefore, the observed intercrystal energy transfer in the red-emitting FAMA PeNC suspension samples can be described by a similar operational mechanism which has the scope to extend the charge transport beyond the diffusion limit and thereby improve the performance for PeNC-based solar cells.

In this work, we successfully synthesized highly stable red -emitting FAMA PeNCs with high PLQYs using a simple hot-addition method. The steady-state PL spectrum of FAMA PeNC can be deconvoluted into two PL bands responsible for the MA (high-energy band) and the FA (low-energy band) domains of the crystal. The PeNC showed remarkable stability for over 30 days, with PLQYs exceeding 80%. For the concentrated sample in a 10 mm cell, the TCSPC decay profiles in the MA domain showed only a decay feature while in the FA domain a nanosecond-rise component appeared together with a slow decay component, with the decay time coefficient increasing upon increasing the probe wavelengths. The nanosecond-rise component disappeared when the solution samples were diluted or in a cell holder with a thinner thickness. The observed nanosecond-rise feature in the concentrated solutions is due to photon recycling when there are nanocrystals nearby feasible for intercrystal energy transfer. The femtosecond FOG and TAS studies were carried out to understand the intracrystal carrier relaxation processes. We found that the hot-carrier charge transfer from MA to the FA domain took ~0.4 ps, while the cold-carrier charge transfer from MA to the FA domain took ~30 ps. The shallow-trap mediated recombination occurred in 10 ps for both MA and FA domains, while the bulk-trap mediated recombination occurred in 60 and 140 ps for MA and FA, respectively. Both FOG and TAS transients involve a nanosecond offset component responsible for the radiative recombination. The TAS profiles showed red shifts of the transient spectra propagating from MA to the FA domain due to the effects of hot carrier cooling and band gap renormalization upon excitation at 400 and 600 nm (MA domain region), whereas no spectral shifts were observed upon excitation at 680 nm (FA domain region). An exciton-hopping model is provided to explain the mechanism of the transient phenomena observed for intercrystal energy transfer (photon recycling), and a carrier relaxation model is provided to interpret the intracrystal charge transfer between the donor MA and the acceptor FA of the FAMA nanocrystals under investigation.

■ ASSOCIATED CONTENT

Supporting Information

The Supporting Information is available free of charge at https://pubs.acs.org/doi/10.1021/acs.jpclett.3c00333.

Experimental methods, Figures S1−S9 (TEM, XRD, PL spectra, PLQY, TCSPC temporal profiles, FOG temporal profiles, and TAS transient spectra and temporal profiles), and Tables S1−S10 (tolerance factor estimation, TCSPC, FOG, TAS, and PLQY curve-fitting results) (PDF)

Transparent Peer Review report available (PDF)

■ AUTHOR INFORMATION

Corresponding Author

Eric Wei-Guang Diau − *Department of Applied Chemistry and Institute of Molecular Science and Center for Emergent Functional Matter Science, National Yang Ming Chiao Tung University, Hsinchu 300093, Taiwan;* orcid.org/0000-0001-6113-5679; Email: diau@nycu.edu.tw

Authors

I-Hua Tsai − *Department of Applied Chemistry and Institute of Molecular Science, National Yang Ming Chiao Tung University, Hsinchu 300093, Taiwan*

Sudhakar Narra − *Department of Applied Chemistry and Institute of Molecular Science and Center for Emergent Functional Matter Science, National Yang Ming Chiao Tung University, Hsinchu 300093, Taiwan;* orcid.org/0000-0003-4893-9204

Sumit S. Bhosale − *Department of Applied Chemistry and Institute of Molecular Science, National Yang Ming Chiao Tung University, Hsinchu 300093, Taiwan*

Complete contact information is available at: https://pubs.acs.org/10.1021/acs.jpclett.3c00333

https://doi.org/10.1021/acs.jpclett.3c00333
J. Phys. Chem. Lett. 2023, 14, 2580−2587

Notes

The authors declare no competing financial interest.

■ ACKNOWLEDGMENTS

This work is supported by the National Science and Technology Council (NSTC), Taiwan (grant nos. NSTC 111-2634-F-A49-007 and NSTC 111-2123-M-A49-001) and the Center for Emergent Functional Matter Science of National Yang Ming Chiao Tung University (NYCU) from The Featured Areas Research Center Program within the framework of the Higher Education Sprout Project by the Ministry of Education (MOE) in Taiwan.

■ REFERENCES

(1) Akkerman, Q. A.; Gandini, M.; Di Stasio, F.; Rastogi, P.; Palazon, F.; Bertoni, G.; Ball, J. M.; Prato, M.; Petrozza, A.; Manna, L. Strongly Emissive Perovskite Nanocrystal Inks for High-Voltage Solar Cells. *Nat. Energy* **2017**, *2*, 16194.

(2) Lin, K.; Xing, J.; Quan, L. N.; Arquer, F. P. G.; de Gong, X.; Lu, J.; Xie, L.; Zhao, W.; Zhang, D.; Yan, C.; Li, W.; Liu, X.; Lu, Y.; Kirman, J.; Sargent, E. H.; Xiong, Q.; Wei, Z. Perovskite Light-Emitting Diodes with External Quantum Efficiency Exceeding 20%. *Nature* **2018**, *562*, 245−248.

(3) Shamsi, J.; Urban, A. S.; Imran, M.; De Trizio, L.; Manna, L. Metal Halide Perovskite Nanocrystals: Synthesis, Post-Synthesis Modifications, and Their Optical Properties. *Chem. Rev.* **2019**, *119*, 3296−3348.

(4) Park, S.; Chang, W. J.; Lee, C. W.; Park, S.; Ahn, H.-Y.; Nam, K. T. Photocatalytic Hydrogen Generation from Hydriodic Acid using Methylammonium Lead Iodide in Dynamic Equilibrium with Aqueous Solution. *Nat. Energy* **2017**, *2*, 16185.

(5) Shyamal, S.; Pradhan, N. Halide Perovskite Nanocrystal Photocatalysts for CO_2 Reduction: Successes and Challenges. *J. Phys. Chem. Lett.* **2020**, *11*, 6921−6934.

(6) Xu, B.; Wang, W. G.; Zhang, X. L.; Cao, W. Y.; Wu, D.; Liu, S.; Dai, H. T.; Chen, S. M.; Wang, K.; Sun, X. W. Bright and Efficient Light-Emitting Diodes based on MA/Cs Double Cation Perovskite Nanocrystals. *J. Mater. Chem. C* **2017**, *5*, 6123−6128.

(7) Tang, X.; Zu, Z.; Shao, H.; Hu, W.; Zhou, M.; Deng, M.; Chen, W.; Zang, Z.; Zhu, T.; Xue, J. All-Inorganic Perovskite $CsPb(Br/I)_3$ Nanorods for Optoelectronic Application. *Nanoscale* **2016**, *8*, 15158−15161.

(8) Protesescu, L.; Yakunin, S.; Bodnarchuk, M. I.; Krieg, F.; Caputo, R.; Hendon, C. H.; Yang, R. X.; Walsh, A.; Kovalenko, M. V. Nanocrystals of Cesium Lead Halide Perovskites ($CsPbX_3$, X = Cl, Br, and I): Novel Optoelectronic Materials Showing Bright Emission with Wide Color Gamut. *Nano Lett.* **2015**, *15*, 3692−3696.

(9) Bhosale, S. S.; Kharade, A. K.; Narra, S.; Chang, S.-m.; Diau, E. W.-G. Self-Photocatalytic Splitting of Carbon Dioxide Using Co-cationic Perovskite Nanocrystals in the Absence of Water. *ACS Energy Lett.* **2023**, *8*, 280−288.

(10) Levchuk, I.; Herre, P.; Brandl, M.; Osvet, A.; Hock, R.; Peukert, W.; Schweizer, P.; Spiecker, E.; Batentschuk, M.; Brabec, C. J. Ligand-Assisted Thickness Tailoring of Highly Luminescent Colloidal $CH_3NH_3PbX_3$ (X = Br and I) Perovskite Nanoplatelets. *Chem. Commun.* **2017**, *53*, 244−247.

(11) Huang, H.; Xue, Q.; Chen, B.; Xiong, Y.; Schneider, J.; Zhi, C.; Zhong, H.; Rogach, A. L. Top-Down Fabrication of Stable Methylammonium Lead Halide Perovskite Nanocrystals by Employing a Mixture of Ligands as Coordinating Solvents. *Angew. Chem.* **2017**, *129*, 9699−9704.

(12) Levchuk, I.; Osvet, A.; Tang, X.; Brandl, M.; Perea, J. D.; Hoegl, F.; Matt, G. J.; Hock, R.; Batentschuk, M.; Brabec, C. J. Brightly Luminescent and Color-Tunable Formamidinium Lead Halide Perovskite $FAPbX_3$ (X = Cl, Br, I) Colloidal Nanocrystals. *Nano Lett.* **2017**, *17*, 2765−2770.

(13) de Weerd, C.; Gomez, L.; Zhang, H.; Buma, W. J.; Nedelcu, G.; Kovalenko, M. V.; Gregorkiewicz, T. Energy Transfer between Inorganic Perovskite Nanocrystals. *J. Phys. Chem. C* **2016**, *120*, 13310−13315.

(14) van der Laan, M.; de Weerd, C.; Poirier, L.; van de Water, O.; Poonia, D.; Gomez, L.; Kinge, S.; Siebbeles, L. D. A.; Koenderink, A. F.; Gregorkiewicz, T.; Schall, P. Photon Recycling in $CsPbBr_3$ All-Inorganic Perovskite Nanocrystals. *ACS Photonics* **2021**, *8*, 3201−3208.

(15) Dupont, E.; Liu, H. C.; Buchanan, M.; Chiu, S.; Gao, M. Efficient GaAs Light-Emitting Diodes by Photon Recycling. *Appl. Phys. Lett.* **2000**, *76*, 4−6.

(16) Giovanni, D.; Righetto, M.; Zhang, Q.; Lim, J. W. M.; Ramesh, S.; Sum, T. C. Origins of the Long-Range Exciton Diffusion in Perovskite Nanocrystal Films: Photon Recycling vs Exciton Hopping. *Light Sci. Appl.* **2021**, *10*, 2.

(17) Pazos-Outon, L. M.; Szumilo, M.; Lamboll, R.; Richter, J. M.; Crespo-Quesada, M.; Abdi-Jalebi, M.; Beeson, H. J.; Vrucinic, M.; Alsari, M.; Snaith, H. J.; Ehrler, B.; Friend, R. H.; Deschler, F. Photon Recycling in Lead Iodide Perovskite Solar Cells. *Science* **2016**, *351*, 1430−1433.

(18) Cho, C.; Zhao, B.; Tainter, G. D.; Lee, J. Y.; Friend, R. H.; Di, D.; Deschler, F.; Greenham, N. C. The Role of Photon Recycling in Perovskite Light-Emitting Diodes. *Nat. Commun.* **2020**, *11*, 611.

(19) Yamada, Y.; Yamada, T.; Kanemitsu, Y. Free Carrier Radiative Recombination and Photon Recycling in Lead Halide Perovskite Solar Cell Materials. *Bull. Chem. Soc. Jpn.* **2017**, *90*, 1129−1140.

(20) Kirchartz, T.; Staub, F.; Rau, U. Impact of Photon Recycling on the Open-Circuit Voltage of Metal Halide Perovskite Solar Cells. *ACS Energy Lett.* **2016**, *1*, 731−739.

(21) de Weerd, C.; Gomez, L.; Capretti, A.; Lebrun, D. M.; Matsubara, E.; Lin, J.; Ashida, M.; Spoor, F. C. M.; Siebbeles, L. D. A.; Houtepen, A. J.; Suenaga, K.; Fujiwara, Y.; Gregorkiewicz, T. Efficient Carrier Multiplication in $CsPbI_3$ Perovskite Nanocrystals. *Nat. Commun.* **2018**, *9*, 4199.

(22) Zeng, M.; Locardi, F.; Mara, D.; Hens, Z.; Van Deun, R.; Artizzu, F. Switching on Near-Infrared Light in Lanthanide-doped $CsPbCl_3$ Perovskite Nanocrystals. *Nanoscale* **2021**, *13*, 8118−8125.

(23) Zheng, W.; Huang, P.; Gong, Z.; Tu, D.; Xu, J.; Zou, Q.; Li, R.; You, W.; Bunzli, J. G.; Chen, X. Near-Infrared-Triggered Photon Upconversion Tuning in All-Inorganic Cesium Lead Halide Perovskite Quantum Dots. *Nat. Commun.* **2018**, *9*, 3462.

(24) Misra, R. K.; Aharon, S.; Li, B.; Mogilyansky, D.; Visoly-Fisher, I.; Etgar, L.; Katz, E. A. Temperature- and Component-Dependent Degradation of Perovskite Photovoltaic Materials under Concentrated Sunlight. *J. Phys. Chem. Lett.* **2015**, *6*, 326−330.

(25) Stoumpos, C. C.; Malliakas, C. D.; Kanatzidis, M. G. Semiconducting Tin and Lead Iodide Perovskites with Organic Cations: Phase Transitions, High Mobilities, and Near-Infrared Photoluminescent Properties. *Inorg. Chem.* **2013**, *52*, 9019−9038.

(26) Yang, J.-N.; Song, Y.; Yao, J.-S.; Wang, K.-H.; Wang, J.-J.; Zhu, B.-S.; Yao, M.-M.; Rahman, S. U.; Lan, Y.-F.; Fan, F.-J.; Yao, H.-B. Potassium Bromide Surface Passivation on $CsPbI_{3-x}Br_x$ Nanocrystals for Efficient and Stable Pure Red Perovskite Light-Emitting Diodes. *J. Am. Chem. Soc.* **2020**, *142*, 2956−2967.

(27) Chiba, T.; Takahashi, Y.; Sato, J.; Ishikawa, S.; Ebe, H.; Tamura, K.; Ohisa, S.; Kido, J. Surface Crystal Growth of Perovskite Nanocrystals via Postsynthetic Lead(II) Bromide Treatment to Increase the Colloidal Stability and Efficiency of Light-Emitting Devices. *ACS Appl. Mater. Interfaces* **2020**, *12*, 45574−45581.

(28) Bhosale, S. S.; Narra, S.; Jokar, E.; Manikandan, A.; Chueh, Y.-L.; Diau, E. W.-G. Functionalized Hybrid Perovskite Nanocrystals with Organic Ligands Showing a Stable 3D/2D Core/Shell Structure for Display and Laser Applications. *J. Mater. Chem. C* **2021**, *9*, 17341−17348.

(29) Li, Z.; Yang, M.; Park, J.-S.; Wei, S.-H.; Berry, J. J.; Zhu, K. Stabilizing Perovskite Structures by Tuning Tolerance Factor: Formation of Formamidinium and Cesium Lead Iodide Solid-State Alloys. *Chem. Mater.* **2016**, *28*, 284−292.

https://doi.org/10.1021/acs.jpclett.3c00333
J. Phys. Chem. Lett. 2023, 14, 2580−2587

(30) Liu, X.; Hong, R.; Tian, C. Tolerance factor and the stability discussion of ABO_3-type ilmenite. *J. Mater. Sci.: Mater. Electron.* **2009**, *20*, 323−327.
(31) Saba, M.; Quochi, F.; Mura, A.; Bongiovanni, G. Excited State Properties of Hybrid Perovskites. *Acc. Chem. Res.* **2016**, *49*, 166−173.
(32) Pan, J.; Shang, Y.; Yin, J.; De Bastiani, M.; Peng, W.; Dursun, I.; Sinatra, L.; El-Zohry, A. M.; Hedhili, M. N.; Emwas, A. H.; Mohammed, O. F.; Ning, Z.; Bakr, O. M. Bidentate Ligand-Passivated $CsPbI_3$ Perovskite Nanocrystals for Stable Near-Unity Photoluminescence Quantum Yield and Efficient Red Light-Emitting Diodes. *J. Am. Chem. Soc.* **2018**, *140*, 562−565.
(33) Tong, Y.; Bladt, E.; Ayguler, M. F.; Manzi, A.; Milowska, K. Z.; Hintermayr, V. A.; Docampo, P.; Bals, S.; Urban, A. S.; Polavarapu, L.; Feldmann, J. Highly Luminescent Cesium Lead Halide Perovskite Nanocrystals with Tunable Composition and Thickness by Ultrasonication. *Angew. Chem.* **2016**, *55*, 13887−13892.
(34) Chen, D.; Li, J.; Chen, X.; Chen, J.; Zhong, J. Grinding Synthesis of $APbX_3$ (A = MA, FA, Cs; X = Cl, Br, I) Perovskite Nanocrystals. *ACS Appl. Mater. Interfaces* **2019**, *11*, 10059−10067.
(35) Lu, Y.-C.; Chang, C.-W.; Diau, E. W.-G. Femtosecond Fluorescence Dynamics of trans-Azobenzene in Hexane on Excitation to the $S_1(n,\pi^*)$ state. *J. Chin. Chem. Soc.* **2002**, *49*, 693−701.
(36) Fu, J.; Xu, Q.; Han, G.; Wu, B.; Huan, C. H. A.; Leek, M. L.; Sum, T. C. Hot carrier cooling mechanisms in halide perovskites. *Nat. Commun.* **2017**, *8*, 1300.
(37) Yang, Y.; Ostrowski, D. P.; France, R. M.; Zhu, K.; van de Lagemaat, J.; Luther, J. M.; Beard, M. C. Observation of a Hot-Phonon Bottleneck in Lead-Iodide Perovskites. *Nat. Photonics* **2016**, *10*, 53−59.
(38) Guo, Z.; Wan, Y.; Yang, M.; Snaider, J.; Zhu, K.; Huang, L. Long-Range Hot-Carrier Transport in Hybrid Perovskites Visualized by Ultrafast Microscopy. *Science* **2017**, *356*, 59−62.
(39) Manser, J. S.; Kamat, P. V. Band Filling with Free Charge Carriers in Organometal Halide Perovskites. *Nat. Photonics* **2014**, *8*, 737−743.
(40) Narra, S.; Bhosale, S. S.; Kharade, A. K.; Chang, S.; Diau, E. W.-G. Retarded Charge Recombination to Enhance Photocatalytic Performance for Water-Free CO_2 Reduction Using Perovskite Nanocrystals as Photocatalysts. *J. Phys. Chem. Lett.* **2022**, *13*, 9134−9139.
(41) Socie, E.; Vale, B. R. C.; Burgos-Caminal, A.; Moser, J. Direct Observation of Shallow Trap States in Thermal Equilibrium with Band-Edge Excitons in Strongly Confined CsPbBr3 Perovskite Nanoplatelets. *Adv. Opt. Mater.* **2021**, *9*, 2001308.

https://doi.org/10.1021/acs.jpclett.3c00333
J. Phys. Chem. Lett. 2023, 14, 2580−2587